Holocene derived from tree-ring data[4].

Our study suggests that comparable cycles in tree growth occurred between interstadials of the last glaciation and today, and hence that similar factors have affected the radial growth of *Fitzroya* since the Late Pleistocene. Considering that the Earth's atmosphere—and the ocean/atmosphere system—were significantly disturbed during the glacial cycles of the Late Pleistocene, the notable similarity in the spectral properties of the Pelluco subfossil and modern *F. cupressoides* chronologies suggests that the forcing mechanisms of climate during the interstadials have not changed dramatically. The potential for developing very long tree-ring chronologies—from the present day back several millennia—is one of the most promising results in southern South America dendrochronology[15,27]. Our Pelluco tree-ring chronology represents a high-resolution window that allows us the possibility of analysing fluctuations in tree growth and climate during warmer events of the last glacial stage in southern Chile, where other very old palaeorecords (>50,000 yr) are rare. □

1. Oldfield, F. (ed.) Global Change Report No. 45 (International Geosphere-Biosphere Programme (IGBP), Stockholm, 1998).
2. Fritts, H. C. *Reconstructing Large-Scale Climatic Patterns from Tree-Ring Data* (Univ. Arizona Press, Tucson, 1991).
3. Pilcher, J. R., Baillie, M. G. L., Schmidt, B. & Becker, B. A 7,272-year tree-ring chronology for western Europe. *Nature* 312, 150–152 (1984).
4. Villalba, R. et al. in *Climate Fluctuations and Forcing Mechanisms of the Last 2,000 Years* (eds Jones, P. D., Bradley, R. S. & Jouzel, J.) 161–189 (Springer, Berlin, 1996).
5. Bradley, R. S. *Quaternary Paleoclimatology* (Chapman & Hall, London, 1992).
6. Clapperton, C. *Quaternary Geology and Geomorphology of South America* (Elsevier, Amsterdam, 1993).
7. Denton, G. H. et al. Geomorphology, stratigraphy, and radiocarbon chronology of Llanquihue Drift in the area of the southern Lake District, Seno Reloncaví, and Isla Grande de Chiloé, Chile. *Geografis. Ann. A* 81, 167–229 (1999).
8. Heusser, C. J., Heusser, L. E. & Lowell, T. V. Paleoecology of the southern Chilean Lake District—Isla Grande de Chiloé during middle—late Llanquihue glaciation and deglaciation. *Geografis. Ann. A* 81, 231–284 (1999).
9. Heusser, C. J. et al. Pollen sequence from the Chilean Lake District during the Llanquihue glaciation in marine oxygen Isotope Stages 4–2. *J. Quat. Sci.* 15, 115–125 (2000).
10. Denton, G. H. et al. Interhemispheric linkage of paleoclimate during the last glaciation. *Geografis. Ann. A* 81, 107–153 (1999).
11. Lara, A. & Villalba, R. A 3620-year temperature record from *Fitzroya cupressoides* tree rings in southern South America. *Science* 260, 1104–1106 (1993).
12. Villalba, R. Tree-ring and glacial evidence for the Medieval Warm Epoch and the Little Ice Age in southern South America. *Clim. Change* 26, 183–197 (1994).
13. Roig, F. A. Dendroklimatologische Untersuchungen an *Fitzroya cupressoides* im Gebiet der Küstenkordillere un der Südlichen Anden. Thesis, Basel Univ. (1996).
14. Miller, A. in *Climates of Central and South America* (ed. Schwerdtfeger, W.) 113–145 (Elsevier, Amsterdam, 1976).
15. Roig, F. A., Roig, C., Rabassa, J. & Boninsegna, J. A. Fuegian floating tree-ring chronologies from sub-fossil *Nothofagus* woods. *Holocene* 6, 469–476 (1996).
16. Lomnitz, C. Major earthquakes and tsunamis in Chile during the period 1535 to 1965. *Geol. Rundsch.* 59, 938–960 (1970).
17. Klohn, C. Beobachtungen über die Reste eines spätzeitlichen Alerceswaldes. *Z. Naturfreunde Wanderer* 1975–1976, 75–78 (1976).
18. Lara, A. The dynamics and disturbance regimes of *Fitzroya cupressoides* forests in the south-central Andes of Chile. Thesis, Univ. Colorado (1991).
19. Porter, S. C. Pleistocene glaciation in the southern Lake District of Chile. *Quat. Res.* 16, 263–292 (1981).
20. Cook, E. R., Briffa, K. R., Shiyatov, S. G. & Mazepa, V. S. in *Methods of Dendrochronology* (eds Cook, E. R. & Kairiukstis, L. A.) 104–123 (Kluwer, Dordrecht, 1990).
21. Cook, E. R., Briffa, K. R., Meko, D. M., Graybill, D. A. & Funkhouser, G. The 'segment length curse' in long tree-ring chronology development for palaeoclimatic studies. *Holocene* 5, 229–237 (1995).
22. Leventer, A. et al. Productivity cycles of 200–300 years in the Antarctic Peninsula region: Understanding linkages among the sun, atmosphere, oceans, sea ice, and biota. *Geol. Soc. Am. Bull.* 108, 1626–1644 (1996).
23. Stuiver, M. & Braziunas, T. F. Atmospheric ¹⁴C and century-scale solar oscillations. *Nature* 338, 405–408 (1989).
24. Lammy, F., Hebbeln, D. & Wefer, G. Late Quaternary precessional cycles of terrigenous sediment input off the Norte Chico, Chile (27.5S) and palaeoclimatic implications. *Palaeogeogr. Palaeoclimatol. Palaeoecol.* 141, 233–251 (1998).
25. Salinger, M. J. Palaeoclimates north and south. *Nature* 291, 106–107 (1981).
26. Markgraf, V. et al. Evolution of late Pleistocene and Holocene climates in the circum-South Pacific land areas. *Clim. Dyn.* 6, 193–211 (1992).
27. Boninsegna, J. A. in *Climate Since A. D. 1500* (eds Jones, P. D. & Bradley, R. S.) 446–462 (Routledge, London, 1992).
28. Jenkins, G. M. & Watts, D. G. *Spectral Analysis and its Applications* (Holden-Day, San Francisco, 1968).
29. Marple, S. L. Jr. *Digital Spectral Analysis with Applications* (Prentice Hall, Englewood Cliffs, New Jersey, 1987).
30. Burg, J. P. in *Modern Spectrum Analysis* (ed. Childers, D. G.) 42–48 (IEEE Press, New York, 1978).
31. Lara, A. et al. in *Dendrochronology in Latin America* (ed. Roig, F. A.) 217–244 (EDIUNC, Mendoza, 2000).

....

Simulating the amplification of orbital forcing by ocean feedbacks in the last glaciation

M. Khodri, Y. Leclainche, G. Ramstein, P. Braconnot, O. Marti & E. Cortijo

LSCE, CE-Saclay, 91191, Gif sur Yvette, France

....

According to Milankovitch theory, the lower summer insolation at high latitudes about 115,000 years ago allowed winter snow to persist throughout summer, leading to ice-sheet build-up and glaciation[1]. But attempts to simulate the last glaciation using global atmospheric models have failed to produce this outcome when forced by insolation changes only[2–5]. These results point towards the importance of feedback effects—for example, through changes in vegetation or the ocean circulation—for the amplification of solar forcing[6–9]. Here we present a fully coupled ocean–atmosphere model of the last glaciation that produces a build-up of perennial snow cover at known locations of ice sheets during this period. We show that ocean feedbacks lead to a cooling of the high northern latitudes, along with an increase in atmospheric moisture transport from the Equator to the poles. These changes agree with available geological data[10–15] and, together, they lead to an increased delivery of snow to high northern latitudes. The mechanism we present explains the onset of glaciation—which would be amplified by changes in vegetation—in response to weak orbital forcing.

Previous simulations using atmosphere general circulation models have shown that the atmosphere alone is unable to produce perennial snow, which is required to start a glaciation[2–7,16]: several studies[3,16] related this failure to model resolution and snow parametrization. However, a major drawback of these simulations was that the ocean surface temperature and vegetation cover were prescribed to their modern values[2–9]. A previous study showed that biosphere–atmosphere interactions help to create favourable conditions for ice-sheet growth[9], but did not succeed in simulating perennial snow cover. For the period of the onset of the last glaciation, studies of planktonic and benthic foraminifera from the North Atlantic Ocean led to the conclusion that the meridional gradient of sea surface temperature (SST) was enhanced before glacial inception—with very cold SST at high latitudes[10] (a cooling of around 4 °C from present-day values) while low latitudes were slightly warmer[10,12] than at present. These studies[10,14,17–19] assumed that the changes in SST pattern were probably due to a shift of deep-water formation from the Norwegian Sea to the North Atlantic. Therefore changes in ocean circulation must have had a large effect on the high-latitude heat budget. These hypotheses remain untested by coupled ocean–atmosphere general circulation models. We tested this possible mechanism for glacial inception using the IPSL-CM2[20] ocean–atmosphere coupled model (see Methods section).

We performed a 100-year-long sensitivity experiment, called here the '115 kyr BP' run, which only differs from the 120-year control experiment in the Earth's orbital parameters, which are set for 115,000 years before present (BP)[21] (Table 1). The concentration of

atmospheric CO_2 is kept at its present level, as found in the Vostok ice-core record[22]. Both simulations are performed without flux corrections and are stable. The changes in the orbital parameters (decreased axial tilt and increased eccentricity) reduce the amplitude of the seasonal cycle of incoming solar radiation at the top of the atmosphere, and produces a 6% decrease of summer insolation over the Northern Hemisphere, compared to the present (Fig. 1a).

These changes in insolation lead to a mean winter surface warming of 3 °C and a summer cooling of 2 °C over the Northern Hemisphere. As shown for the mid-Holocene[20] (6 kyr BP), the seasonal surface air temperature over land mimics the insolation

forcing with no lag in time (Fig. 1b), whereas the response of the ocean surface temperature is delayed by about 2–3 months (Fig. 1c). This time lag enhances the Equator-to-pole thermal gradient in summer, particularly over the North Atlantic where subtropical latitudes are warmer and high latitudes colder (Fig. 2a, b). The insolation changes and the colder surface ocean temperatures in the northern high latitudes also prevent the melting of sea ice in
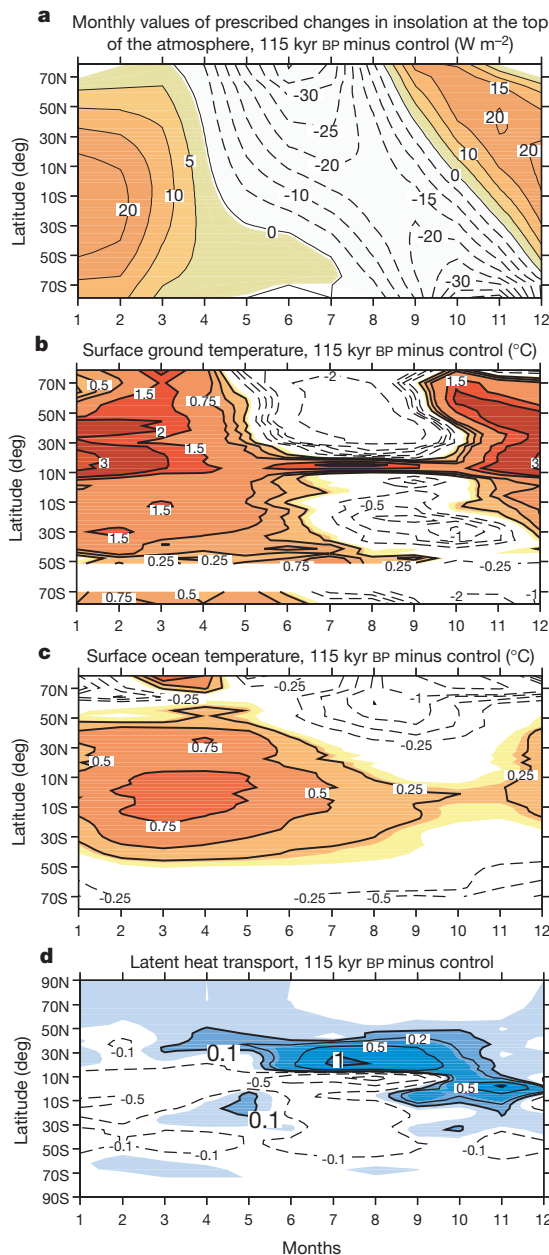
Figure 1 Seasonal variations of the response of surface temperature and the hydrological cycle to changing insolation forcing at the top of the atmosphere. **a**, **b**, Zonal-mean difference between 115 kyr BP and control simulations: **a**, for incoming solar radiation at the top of the atmosphere; **b**, for ground surface temperature; **c**, for sea surface temperature; and **d**, for northward latent heat transport over the Atlantic Ocean. Contour intervals are every 5.0 W m^{-2} in **a**, every 0.25 °C in **b** and **c**, and every 0.1 PW (10^{15} W) in **d**, with negative values as dotted lines in all panels. Month 1 is January.
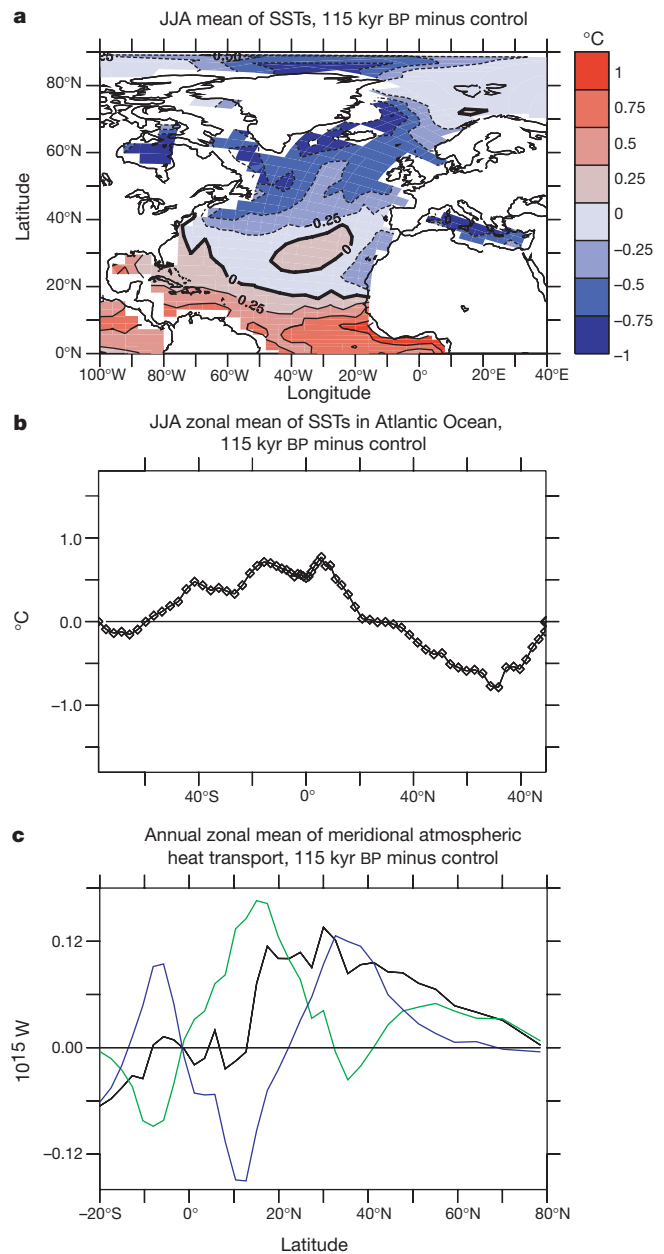
Figure 2 Changes in sea surface temperature and heat transport in response to seasonal perturbation in solar forcing. **a**, Difference between June–August means of sea surface temperature (SST) over the North Atlantic in the 115 kyr BP and control simulations. Contour intervals are every 0.25 °C, with negative values as dashed lines. **b**, Difference between June–August zonal means of Atlantic sea surface temperature in the 115 kyr BP and control simulations. The enhanced Atlantic Ocean surface temperature gradient in the Northern Hemisphere summer in the 115 kyr BP experiment compared to the control run is robust, considering the low amplitude of the inter-decadal variability of SST in the control experiment. **c**, Zonal mean difference between the 115 kyr BP and control simulations of the Equator-to-pole atmospheric heat transport in PW, for total (black line), dry static (green line) and latent (blue line). We note that there is a 6% increase of northward latent-heat transport in comparison with the control run.

summer, and lead to an increased mean sea-ice volume in the Northern Hemisphere (from 21×10^3 km^3 in the control experiment, to 30×10^3 km^3 for the 115 kyr BP run), which constitutes a further feedback for high-latitude cooling. The amplified summer gradient over the North Atlantic Ocean is in good agreement with SSTs inferred from marine data[10,12,14]. The annual mean temperature shows the continents in the Northern Hemisphere to be 1 °C warmer, except for northeastern Canada, Greenland, western Europe and northern Siberia, which are about 0.5 °C cooler. This annual mean surface temperature pattern, which results from a

seasonal perturbation with marked latitudinal structure, is reasonable when compared to data for the end of the last interglacial[23,24].

The thermohaline circulation of the ocean is also affected by the orbital forcing. In the control simulation, deep-water convection occurs during winter in the Norwegian–Greenland seas and to the south and west of Iceland, with a maximum reached in March[25]. The deep sinking of surface water at around 60° N is associated with the northward advection of relatively warm and salty waters by the North Atlantic drift to the Norwegian–Greenland–Iceland seas (GIN seas). In the 115 kyr BP experiment, the convection is less active in the GIN seas as shown by the shallower mixed-layer depth there (Fig. 3c). This deep mixing is however slightly shifted southward in the North Atlantic. Deep mixing also disappears in March, leading to a shortened season of deep-water formation. The North Atlantic meridional overturning at 2,000 m depth is therefore weakened by about 2 Sv, and the North Atlantic Deep Water (NADW) is shallower (Fig. 3a, b), confirming that the thermohaline circulation is very sensitive to external forcings[26]. However, the maximum of the Atlantic overturning function is the same as the value in the control simulation (about 14 Sv), showing that the thermohaline circulation is still active—in agreement with data[15].

The spreading of deep convection in the North Atlantic, with formation of much shallower NADW—which has been much discussed[10,14]—appears to be induced, in our simulation, by two mechanisms. First, the summer increase of the Equator-to-pole surface temperature gradient (Fig. 2a, b) acts to enhance the annual northward transport of moisture by the atmosphere (Figs 1d, 2c). Precipitation is therefore enhanced over land, leading to a 14% annual mean increase of the Siberian river runoff into the Arctic Ocean, which in turn reduces the salinity (−0.2‰) of waters advected to the sinking sites in winter. This southward extension of the cold and less-salty Greenland current from the northern seas in winter, at the expense of the northward extension of the warm water, causes the reduction of surface salinity and temperature south of the Denmark Strait (near 60° N) despite the warmer North Atlantic induced by primary solar forcing. Second, the warmer winter continent surface together with this local winter cooling of surface waters attenuates the atmospheric stationary waves in January and February. The consequence is a decreased Icelandic low and a reduction of the pressure gradient between Iceland and Spitzberg over the Atlantic Ocean. The associated weaker cyclonic activity reduces the northeast extension of the warmer and saltier water from the North Atlantic into the Norwegian Sea. Consequently this favours the southward shift of the polar front and the reduction of water exchange between the North Atlantic and the Arctic Ocean, and therefore favours increased deep mixing in the North Atlantic at the expense of the GIN seas.

The ocean therefore induces strong positive feedbacks to the primary insolation forcing. It amplifies the initial response of surface temperature to the meridional gradient of insolation, both in latitude and time (Fig. 1a, c). This increases the annual northward atmospheric heat transport by about 4% (Fig. 2c). The maximum increase of atmospheric heat transport to the north is primarily due to latent heat transport (Fig. 2c), enhancing water transport over high latitudes of the Northern Hemisphere. The response of the
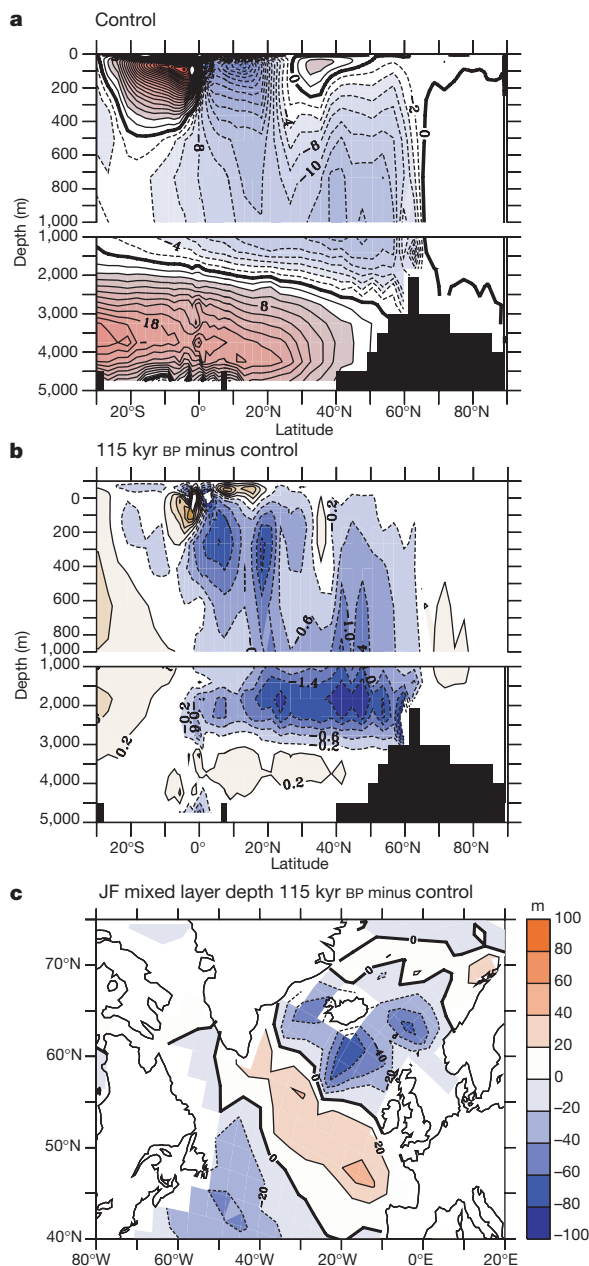
Figure 3 Response of thermohaline circulation and deep convection to changing insolation forcing. **a**, **b**, Latitude–depth distribution of the annual mean Atlantic stream function in sverdrups (Sv) for **a**, the control experiment and **b**, the difference between 115 kyr BP and control. **c**, Difference between January–February means of the mixed layer depth in the North Atlantic for the 115 kyr BP and control simulations. Contour intervals are every 20 m, with negative values shown as dashed lines. We note the deepening of the mixed layer depth in the North Atlantic Ocean (at 50 °N) where active deep-water flow takes over from the Norwegian/Greenland sinking site (at 60 °N).

Table 1 Orbital parameters of the Earth used in the coupled simulation

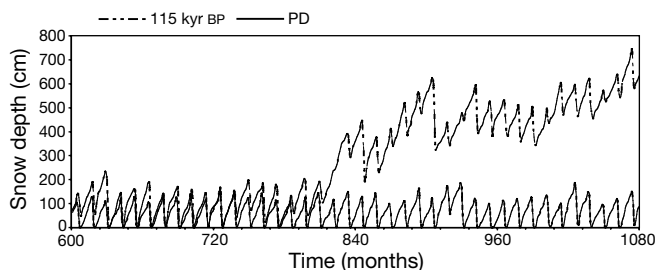|	Control	115 kyr BP
Eccentricity	0.016724	0.041421
Obliquity (axial tilt, °)	23.446	22.404
Perihelion −180° (°)	102.04	110.88
Integration time (yr)	120	100

These parameters were used for calculation of incoming solar radiation at the top of the atmosphere for the control and for the 115 kyr BP experiment. Time integration: for both simulations the oceanic drift in terms of global mean SST is about 0.25 °C per century. The similarity of the drift for those simulations allows the comparison of the two resulting climates. Our analyses are based on a 70-year running mean of annual cycles.

Atlantic thermohaline circulation, in contrast to that of the atmosphere, is not directly to the amplified meridional solar forcing. By analogy with the circulation of the modern Atlantic, which acts to reduce the Equator-to-pole temperature gradient, we would expect an increased poleward ocean heat flux in the 115 kyr BP configuration. However, the equilibrium response of the NADW to changes in the winds and the hydrological cycle is such that the oceanic heat transport from low to high latitudes decreases by about 6%.

The enhanced high-latitude cooling of the Northern Hemisphere, together with the increased atmospheric moisture transport, provide optimal conditions for delivering snow over the Northern Hemisphere. This ocean–atmosphere adjustment in our simulation is the main feedback that occurs under the insolation conditions of the last glacial inception. Snow becomes perennial over the Canadian archipelagos. In these regions, snow accumulates through time in the 115 kyr BP run for two reasons. First, because of the increased summer snowfall (by about 63.5%), and second, because of the persistence of snow in summer (due to the cooling and the slight northward shift of the circulation of the atmosphere; Fig. 4). There is also a tendency for snow accumulation in northern Norway and in northeastern Europe, which are thought to be the nucleation sites for the Fennoscandian ice sheet[27,28]. Moreover, perennial snow cover simulated over the Canadian Arctic islands is consistent with data[29], according to which initial snow accumulation over Fennoscandia began after the ice sheets had built-up over North America.

The role of ocean dynamics—through the rearrangement of North Atlantic deep convection—in triggering the last glacial inception is commonly assumed when interpreting palaeoclimate data[10,14,17–19]. The main strength of our coupled model simulation is that it illustrates the role of the ocean in modifying the seasonal insolation forcing factor, both in time and amplitude. This produces significant changes in surface temperatures and deep-water production, leading to perennial snow over northeastern Canada, in good agreement with data. We have shown that in simulations, before accumulating snow and then triggering the albedo feedback, it is necessary to account for complex feedback mechanisms involving atmospheric winds, the hydrological cycle and ocean dynamics, which allow an increase of snow delivery and persistence in summer over high latitudes. We did not consider biosphere–atmosphere interactions; but such interactions would lead to further cooling by enhancing the surface albedo of high latitudes[9], thus favouring the onset of glaciation. For this reason, biosphere–atmosphere interactions need to be considered in future work. Our results confirm the considerable effects that modifications of ocean dynamics can have on the climate of the Northern Hemisphere middle and high latitudes; this may help to shed light on the potential role of ocean dynamics in future climate changes. □

Figure 4 Monthly time series of snow depth in centimetres. Time starts from January of year 50 for the control experiment (solid line) and for the 115 kyr BP experiment (dashed line) at a glaciation-sensitive region in the Laurentide area (70° N; 80° W). We see that seasonality is important. Snow depth is very stable all along the control run, with no snow in summer, whereas the 115 kyr BP run shows an increase of snow depth associated with perennial snow cover beginning at year 80 and lasting until the end of the run.

Methods

The IPSL-CM2 ocean–atmosphere coupled model is an improved version of the IPSL-CM1 ocean–atmosphere coupled model[20]. The atmospheric model has a resolution of about 400×400 km at 50° latitude. The atmospheric component includes an improved version of the SECHIBA land-surface scheme[20]. The ocean component horizontal mesh is orthogonal and curvilinear on the sphere. The northern point of the convergence has been shifted onto Asia, in order to overcome the singularity of Northern Hemisphere high latitudes. The ocean model spatial resolution over high latitude reaches a maximum size of 4° by 3°. This version of the model includes a complex sea-ice model, with three different ice types having specific thermodynamic behaviour[25]. A variable fraction of leads in the sea-ice cover is simulated. Dynamical process are however not represented. The Northern Hemisphere sea-ice cover and seasonal cycle is realistic. Maximum (13.7×10^6 km^2) and minimum (7.5×10^6 km^2) ice extent are in the range of satellite estimates (13.5×10^6 km^2 and 6×10^6 km^2 respectively)[25]. In the present-day climate simulation, this complex thermodynamic sea-ice model has a large effect on the characteristics of water masses in the Arctic, in the GIN seas, and over deep convection. This model controls in part the seasonality of surface water salinity, as it simulates brine rejection during ice formation and release of fresh water during ice melting. The higher salinity in winter together with the cooling allows deep convection over the GIN seas, and a deep-water flow through the Denmark Strait of about 6.1 Sv—which is in good agreement with the estimates of about 6 Sv (ref. 30). In turn, this convection strengthens surface advection, and the annual mean maximum of the overturning function in the North Atlantic, which is about 14.6 Sv. Accumulation of snow, its transformation into ice due to snow flooding, the evolution of snow surface albedo with snow age, and specific albedos for frozen and melted ice, are all represented in the model. The two models exchange ocean and sea-ice surface temperatures, sea-ice cover, sea-ice albedo, momentum, heat and fresh water fluxes once a day[20]. The 115 kyr BP experiment is a 100-year simulation, starting from year 40 of the control run by simply switching the Earth's orbital parameters to those valid for 115 kyr BP. For both simulations, the oceanic drift in terms of SST is only about 0.22 °C per century, despite the no-flux correction.

Precipitation falls as snow in the model, if the air temperature above the surface is less than 0 °C. Snow cover and snow age affect the surface albedo over land and the heat capacity of the surface. Albedos due to snow cover also vary with surface type (with or without vegetation). Sublimation of snow is calculated as part of the surface evaporative flux, and snowmelt contributes to soil moisture. At the surface of snow-covered grid points, the net heat gain is used to heat snow until it reaches the freezing point (0 °C) and the excess heat gain is used to melt snow. Our modern climate experiment with this snow parametrization shows snow cover, repartition and seasonal variation in the Northern Hemisphere in good agreement with climatology, which is a necessary precondition for glacial inception studies.

1. Milankovitch, M. K. Kanon der erdbestrahlung une seine anwendung anf daseiszeitenproblem. *Serb. Acad. Beorg. Spec. Publ.* **132**, (1941) (in Yugoslavian); Canon of Insolation and the Ice Age Problem (Israel Program for Scientific Translation, Jerusalem, 1969) (English transl.).
2. Royer, J. F., Deque, M. & Pestiaux, P. Orbital forcing of the inception of the Laurentide ice sheet? *Nature* **304**, 43–46 (1983).
3. Rind, D., Peteet, D. & Kukla, G. Can Milankovitch orbital variations initiate the growth of ice sheets in a general circulation model? *J. Geophys. Res.* **94**, 12851–12871 (1989).
4. Oglesby, R. J. Sensitivity of glaciation to initial snow cover, CO₂, snow albedo, and oceanic roughness in the NCAR GCM. *Clim. Dyn.* **4**, 219–235 (1990).
5. Mitchell, J. F. B. Modelling of paleoclimates: examples from the recent past. *Phil. Trans. R. Soc. Lond. B* **341**, 267–275 (1993).
6. Dong, B. & Valdes, P. J. Sensitivity studies of northern hemisphere glaciation using an atmospheric general circulation model. *J. Clim.* **8**, 2471–2495 (1995).
7. Phillipps, P. J. & Held, M. The response to orbital perturbations in a atmospheric model coupled to a slab ocean. *J. Clim.* **7**, 767–782 (1994).
8. Gallimore, R. G. & Kutzbach, J. E. Role of orbitally induced changes in tundra area in the onset of glaciation. *Nature* **381**, 503–505 (1996).
9. DeNoblet, N. *et al.* Possible role of atmosphere-biosphere interactions in triggering the last glaciation. *Geophys. Res. Lett.* **23**, 3191–3194 (1996).
10. Cortijo, E. *et al.* Changes in meridional temperature and salinity gradients in the North Atlantic Ocean (30°-72°N) during the last interglacial period. *Paleoceanography* **14**, 23–33 (1999).
11. Duplessy, J. C. & Shackleton, N. J. Response of global deep-water circulation to Earth's climatic change 135,000-107,000 years ago. *Nature* **316**, 500–507 (1985).
12. Ruddiman, W. F. & McIntyre, A. Warmth of the subpolar North Atlantic ocean during Northern Hemisphere ice-sheet growth. *Science* **204**, 173–175 (1979).
13. Adkins, J. F., Boyle, E. A., Keigwin, L. & Cortijo, E. Variability of the North Atlantic thermohaline circulation during the last interglacial period. *Nature* **390**, 154–156 (1997).
14. Cortijo, E. *et al.* Eemian cooling in the Norwegian Sea and North Atlantic ocean preceding continental ice-sheet growth. *Nature* **372**, 446–449 (1994).
15. Duplessy, J. C. & Shackleton, N. J. Deepwater source variations during the last climatic cycle and their impact on ocean deep water circulation. *Paleoceanography* **3**, 343–360 (1988).
16. Marshall, S. J. & Clarke, G. K. C. Ice sheet inception: Subgrid hypsometric parameterization of mass balance in an ice sheet model. *Clim. Dyn.* **15**, 533–550 (1999).
17. Imbrie, J. *et al.* On the structure and origin of major glaciation cycles, 1. Linear responses to Milankovitch forcing. *Paleoceanography* **7**, 701–738 (1992).
18. Imbrie, J. *et al.* On the structure and origin of major glaciation cycles, 2. The 100,000-year cycle. *Paleoceanography* **8**, 669–735 (1993).
19. Balbon, E. *Variabilité Climatique et Circulation Thermohaline dans l'océan Atlantique Nord et en Mer de Norvège au Cours du Dernier Quaternaire Supérieur.* Thesis, Orsay Univ. (2000).
20. Braconnot, P., Marti, O., Joussaume, S. & Leclainche, Y. Ocean feedback in response to 6kyr BP insolation. *J. Clim.* **13**, 1537–1553 (2000).

21. Berger, A. Long term variation of daily insolation and Quaternary climatic changes. *J. Atmos. Sci.* **35**, 2362–2367 (1978).

22. Raynaud, D. *et al.* The ice record of greenhouse gases. *Science* **259**, 926–934 (1993).

23. LIGA members. The last interglacial in high latitudes of the northern hemisphere: Terrestrial and marine evidence. *Quat. Int.* **10–12**, 9–28 (1991).

24. Sànchez Goñi, M. F., Eynaud, F., Turon, J. L. & Shackleton, N. J. High resolution palynological record off the Iberian margin: direct land-sea correlation for the last interglacial complex. *Earth Planet. Sci. Lett.* **171**, 123–137 (1999).

25. Leclainche, Y. *et al.* Diagnostic versus thermodynamic sea ice models in global coupled ocean-atmosphere simulations. *Clim. Dyn.* (submitted).

26. Rahmstorf, S. Bifurcation of the Atlantic thermohaline circulation in response to changes in the hydrological cycle. *Nature* **378**, 145–149 (1995).

27. Ives, J. D., Andrews, J. T. & Barry, R. G. Growth and decay of the Laurentide ice sheet and comparison with Fenno-Scandinavia. *Naturwissenschaften* **2**, 118–125 (1975).

28. Andrews, J. T. & Mahafy, M. A. W. Growth rates of the Laurentide ice sheet and sea level lowering (with emphasis on the 115,000 B.P. sea level low). *Quat. Res.* **6**, 167–183 (1976).

29. Mangerud, J. in *Klimageschichtliche Probleme der letzten 130,000 Jahre* (ed. Frenzel, B.) 307–330 (Fisher, Stuttgart, 1991).

30. Schmitz, W. J. & McCartney, M. S. On the North Atlantic circulation. *Rev. Geophys.* **31**, 29–49 (1993).

....

Late Jurassic salamanders from northern China

Ke-Qin Gao* & Neil H. Shubin†

* *American Museum of Natural History, Central Park West at 79th Street, New York, New York 10024, USA*

† *Department of Organismal Biology and Anatomy, University of Chicago, 1027 East 57th Street, Chicago, Illinois 60637, USA*

....

With ten extant families, salamanders (urodeles) are one of the three major groups of modern amphibians (lissamphibians)[1–6]. Extant salamanders are often used as a model system to assess fundamental issues of developmental, morphological and biogeographical evolution[6–11]. Unfortunately, our understanding of these issues has been hampered by the paucity of fossil evidence available to assess the early history of the group[5,6,12]. Here we report the discovery of an extraordinary sample of salamander fossils, some with rare soft-tissue impressions, from the Upper Jurassic of China[13–16]. With over 500 articulated specimens, this assemblage documents the morphological diversity of early urodeles and includes larvae and adults of both neotenic and metamorphosed taxa. Phylogenetic analysis confirms that these salamanders are primitive, and reveals that all basal salamander clades have Asian distributions. This is compelling evidence for an Asian origin of Recent salamanders, as well as for an extensive and early radiation of several major lineages. These discoveries show that the evolution of salamanders has involved phylogenetic and ecological diversification around a body plan that has remained fundamentally stable for over 150 million years.

Amphibia Linnaeus, 1758
Lissamphibia Haeckel, 1866
Caudata Scopoli, 1777
Urodela Dumeril, 1806
Family incertae sedis
Sinerpeton fengshanensis gen. et sp. nov.

Holotype. GMV 1606, articulated skeleton including cranium and postcranium.

**Etymology.** *Sino* + *herpeton* (Greek, meaning creeping animal from China); fengshan (the type locality).

Type locality and horizon. Fengshan, Hebei Province, China; Late Jurassic fossil beds that overlay the Zhangjiakou Formation (Tithonian)[13–16].

Referred material. GMV 1607–1610, and numerous unnumbered topotypic specimens.

Diagnosis. *S, fengshanensis* is a neotenic form that retains primitive urodele characters including: small dorsal processes on paired premaxillae; paired nasals articulated in midline; the presence of separate angular and coronoid; and a basale commune representing fused distal carpals 1+2 in the manus. It shares derived characters such as unicapitate ribs with cryptobranchoids, but differs from this group in having the following combination of characters: presacral vertebrae with laterally expanded zygapophyses; a single centrale; a greatly expanded metacarpal II in the manus; and phalangeal formulae of 1-2-3-2 in manus and 1-2-3-4-2 in pes.

The Fengshan assemblages include articulated specimens of both neotenic (*S. fengshanensis*; Figs 1, 2) and fully metamorphic salamanders (*Laccotriton subsolanus*; Fig. 3)[17]. The holotype of the new taxon *Sinerpeton* retains an ossified mesopodium and paired ossified ceratobranchials; the combination of these features suggests that this specimen represents a mature individual with external gills. The assessment of *L. subsolanus* as a metamorphic form is based on its high degree of ossification, particularly in the mesopodium, and apparent lack of external gills—ossified ceratobranchials are absent in adults (Fig. 3). Larvae are also present in the Fengshan sample. These specimens, some of which preserve impressions of the soft tissues of the external gills, have weakly ossified skeletons, are smaller than the metamorphosed individuals of *Laccotriton*, and retain the distinctive skull proportions seen in many larval salamanders (Fig. 3).

The 500-plus articulated salamander skeletons from the Fengshan locality were recovered from a small area of no more than 10 m². The high concentration of fully articulated specimens in tuffaceous shales indicates catastrophic mass mortality during a pyroclastic eruption. The age of the fossil beds is probably mid-Tithonian or slightly younger, on the basis of radiometric dating and biostratigraphy. The underlying Zhangjiakou Formation yields an ^{40}Ar/^{39}Ar
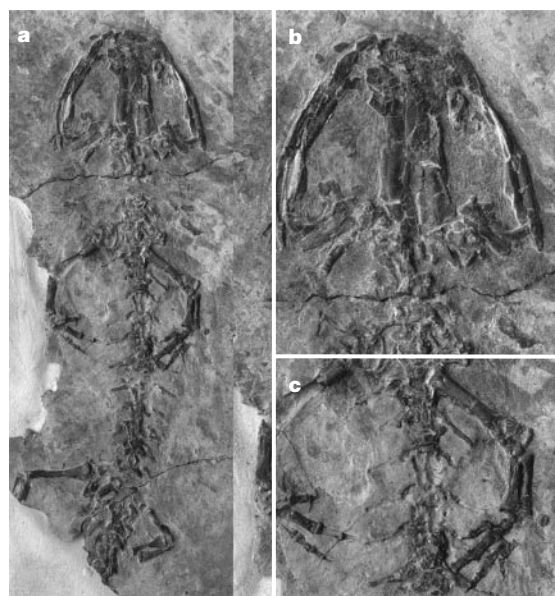
Figure 1 Holotype (GMV 1606) of *S. fengshanensis*, gen. et sp. nov. **a**, Dorsal view of articulated skeleton including the cranium and postcranium. **b**, Enlarged skull. **c**, Enlarged pectoral girdle and forelimbs.